

Article

# Comparing the Photocatalytic Oxidation Efficiencies of Elemental Mercury Using Metal-Oxide-Modified Titanium Dioxide under the Irradiation of Ultra-Violet Light

Ji-Ren Zheng and Chung-Shin Yuan \*

Institute of Environmental Engineering, National Sun Yat-Sen University, No. 70, Lian-Hai Road, Kaohsiung 80424, Taiwan; d103030008@nssysu.edu.tw

\* Correspondence: ycsngi@mail.nsysu.edu.tw; Tel.: +886-7-5252000

**Abstract:** Since the signing of the Minamata Convention in 2013, attempts have been primarily focused on reducing the emission of elemental mercury ( $Hg^0$ ) from coal-fired power plants (CFPPs). The most cost-effective measure for controlling the emission of mercury involves oxidizing  $Hg^0$  to mercury oxides, which are then removed using wet flue gas desulfurization (WFGD). Thus, novel photocatalysts with the best properties of photocatalytic ability and thermal stability need to be developed urgently. In this study, titanium dioxide ( $TiO_2$ )-based photocatalysts were synthesized through the modification of three metal oxides: CuO,  $CeO_2$ , and  $Bi_2O_3$ . All the photocatalysts were further characterized using X-ray diffraction, X-ray photoelectron spectroscopy, photoluminescence, and ultraviolet-visible spectrometry. The photocatalytic oxidation efficiencies of  $Hg^0$  were evaluated under an atmosphere of  $N_2 + Hg^0$  at 100–200 °C. The photocatalytic reactions were simulated by kinetic modeling using the Langmuir–Hinshelwood (L–H) mechanism. The results showed that  $Bi_2O_3/TiO_2$  exhibited the best thermal stability, with the best oxidation efficiency at 200 °C and almost the same performance at 100 °C. L–H kinetic modeling indicated that photocatalytic oxidation reactions for the tested photocatalysts were predominantly physical adsorption. Additionally, the activation energy ( $E_a$ ), taking into account Arrhenius Law, decreased dramatically after modification with metal oxides.



**Citation:** Zheng, J.-R.; Yuan, C.-S. Comparing the Photocatalytic Oxidation Efficiencies of Elemental Mercury Using Metal-Oxide-Modified Titanium Dioxide under the Irradiation of Ultra-Violet Light. *Catalysts* **2024**, *14*, 209. <https://doi.org/10.3390/catal14030209>

Academic Editors: Sylwia Mozia and Roberto Fiorenza

Received: 7 February 2024  
Revised: 16 March 2024  
Accepted: 18 March 2024  
Published: 20 March 2024



**Copyright:** © 2024 by the authors. Licensee MDPI, Basel, Switzerland. This article is an open access article distributed under the terms and conditions of the Creative Commons Attribution (CC BY) license (<https://creativecommons.org/licenses/by/4.0/>).

**Keywords:** elemental mercury;  $TiO_2$ ; metal oxide modification; photocatalytic oxidation; L–H kinetic modeling

## 1. Introduction

According to the United Nations Environment Programme, the estimated mercury emissions from coal-fired power plants (CFPPs) exceed 30% of total anthropogenic mercury emissions [1]. Mercury (Hg) is recognized as a metallic pollutant with detrimental effects on human beings and ecosystems due to its biochemical properties of bioaccumulation and biomagnification [2]. After the signing of the Minamata Convention in 2013, the control of mercury emissions from CFPPs was treated as the primary target for reducing elemental mercury ( $Hg^0$ ) emission into the atmosphere. Currently, constructed CFPPs have to adopt the best available control technologies and the best environmental practices according to the Minamata Convention on Mercury [3].

The typical mercury species normally consists of three basic forms: elementary, oxidized, and particulate. Among these,  $Hg^0$  accounts for the largest proportion [4]. Particulate mercury can be removed by particle collectors such as the electrostatic precipitator (ESP) and fabric filter. Oxidized mercury can be either adsorbed on a fly ash surface and then removed by particle collectors, or dissolved in an absorbent and removed using wet flue gas desulfurization (WFGD) [5].  $Hg^0$  is highly volatile in ambient air and insoluble in water. It can be adsorbed by activated carbon (AC) or carbon black or further oxidized to mercury oxides and then dissolved via WFGD [6]. Using adsorbents such as AC requires

the installation of extra air pollution control devices, which require high maintenance and involve high costs [7].

As a result, previous studies proposed an economical method for reducing mercury emissions by adding oxidative catalysts in selective catalytic reduction (SCR) to progress the potential catalytic oxidation of  $Hg^0$  [8]. However, there is an urgent need to resolve several obstacles in the catalytic oxidation process in SCR. The optimal temperature for existing SCR catalysts is 300–400 °C, which, unfortunately, is a fatal defect in the photocatalytic oxidation of  $Hg^0$  as its optimal operating temperature is below 100 °C [9]. Moreover, to avoid installing extra heating devices, SCR devices are commonly installed upstream of particle collectors (i.e., ESP), which mostly contain high-concentration particulate matter causing a masking effect over the surface of catalysts and reducing their catalytic activity and lifetime [10]. Therefore, it is crucial to develop a low-temperature SCR catalyst operating at 100–200 °C to achieve the goal of moving the SCR behind the particle collector [11].

TiO<sub>2</sub> is the most commonly used photocatalyst due to its advantages of non-toxicity, high oxidation activity, good chemical and thermal stabilities, and low cost. However, the operating temperature of pristine TiO<sub>2</sub> is too low for direct use in industrial applications. Thus, numerous methods have been developed to modify TiO<sub>2</sub> by employing metal oxide [12], graphene [13], metal–organic frameworks [14], and zeolite [15]. Among these, the modification of metal oxide is the simplest method for effectively enhancing TiO<sub>2</sub> activity by retarding the recombination of photo-induced electron/hole pairs, decreasing the energy bandgap, and/or increasing light absorptivity. The metal modification can be classified as either single metal atom doping with Au, Ag, and Pt or metal oxide modification with CuO<sub>2</sub>, MnO<sub>2</sub>, Fe<sub>2</sub>O<sub>3</sub>, CeO<sub>2</sub>, and Bi<sub>2</sub>O<sub>3</sub> [16,17]. In particular, the radius of Cu<sup>2+</sup> is 0.073 nm, which is close to that of Ti<sup>4+</sup> (0.068 nm). Thus, Cu might enter the TiO<sub>2</sub> molecular structure, which is beneficial for separating the photo-induced electron/hole pairs [18]. Wu et al., (2015) reported that TiO<sub>2</sub> did not exhibit any photocatalytic activity on  $Hg^0$  under visible light. The modification of 1.25 weight % CuO had 57.8% photocatalytic oxidation efficiency of  $Hg^0$  under sunlight and 85% under UV light [19]. Another potential modifying material is CeO<sub>2</sub>; the oxygen vacancies in CeO<sub>2</sub> can form active sites and capture either  $Hg^0$  or oxygen atoms from the gas steam. Additionally, CeO<sub>2</sub>/TiO<sub>2</sub> shows strong thermal stability at high temperatures of 160–250 °C. This is mainly due to the conversion of the valence states of Ce(II)O<sub>2</sub> to Ce(III)<sub>2</sub>O<sub>3</sub> ( $2 CeO_2 + Hg^0 \rightarrow Ce_2O_3 + HgO$ ). The consumed oxygen can be recovered by Ce<sup>3+</sup>, which captures O<sub>2</sub> molecules from the gas stream, accelerating the oxidation of  $Hg^0$  [20]. Li et al. (2011) reported that 1.5% CeO<sub>2</sub>/TiO<sub>2</sub> could reach 90% at 250 °C related to the weakly bonded oxygen and chemisorbed oxygen on Ce<sup>3+</sup> [21]. TiO<sub>2</sub> responds solely to UV<sub>A</sub>, thus its overall light absorptivity is relatively low because it does not respond to visible light. Therefore, adding visible-light-responsive additives to TiO<sub>2</sub> might potentially enhance the catalytic oxidation of  $Hg^0$ . With its low energy band gap (2.85 eV), Bi<sub>2</sub>O<sub>3</sub> is one of the potential materials for increasing the light adsorption ability [22].

In this study, we chose three metal oxides (CuO, CeO<sub>2</sub>, and Bi<sub>2</sub>O<sub>3</sub>) to synthesize TiO<sub>2</sub>-based photocatalysts with the aim of enhancing the photocatalytic oxidation of  $Hg^0$  at higher temperatures. This study analyzed the characteristics of self-prepared photocatalysts and conducted photocatalytic oxidation experiments to evaluate the photocatalytic oxidation efficiencies of  $Hg^0$  in an N<sub>2</sub> + O<sub>2</sub> atmosphere. Furthermore, the pros and cons of three metal-oxide-modified TiO<sub>2</sub> photocatalysts were also evaluated.

## 2. Results and Discussion

### 2.1. Characterization of Photocatalysts

Figure 1 illustrates the nitrogen adsorption–desorption isotherms of the photocatalysts. It shows that there is no overlap between the adsorption and desorption curves of all photocatalysts presenting type IV isotherm species according to the International Union of Pure and Applied Chemistry isothermal classification. The type IV isotherm, with a capillary effect resulting in the hysteresis loop, is usually observed in mesoporous materials [23].

A more detailed examination of the hysteresis loop revealed that  $\text{TiO}_2$ ,  $\text{CeO}_2/\text{TiO}_2$ , and  $\text{CuO}/\text{TiO}_2$  had a type H2 loop that contributed to the complex pore structure, with the pores in the shape of ink bottles [24]. The desorption curve of  $\text{CuO}/\text{TiO}_2$  showed a steep desorption branch at a lower relative pressure region, indicating a smaller pore diameter of  $\text{CuO}/\text{TiO}_2$ . Further,  $\text{Bi}_2\text{O}_3/\text{TiO}_2$  showed a H3-type hysteresis loop with a lower limit of the desorption branch located at the cavitation-induced  $P/P_0$ . This phenomenon showed that the average pore diameter of  $\text{Bi}_2\text{O}_3/\text{TiO}_2$  was larger than those of  $\text{TiO}_2$ ,  $\text{CeO}_2/\text{TiO}_2$ , and  $\text{CuO}/\text{TiO}_2$ . Table 1 summarizes the specific surface areas (SSAs) and average pore diameters of the photocatalysts. The SSAs of the photocatalysts were in the order  $\text{TiO}_2 > \text{Bi}_2\text{O}_3/\text{TiO}_2 > \text{CeO}_2/\text{TiO}_2 > \text{CuO}/\text{TiO}_2$ , while the average pore diameters were in the order  $\text{Bi}_2\text{O}_3/\text{TiO}_2 > \text{CeO}_2/\text{TiO}_2 > \text{TiO}_2 > \text{CuO}/\text{TiO}_2$ . Because  $\text{Bi}_2\text{O}_3/\text{TiO}_2$  had the highest SSA among the three metal-oxide-modified photocatalysts, it could have more active sites over the surface of inner pores to adsorb the reactant ( $\text{Hg}^0$ ). Additionally, it had a larger pore diameter, which could more easily move the desorbed product ( $\text{HgO}$ ) out of the photocatalyst through its inner pore passages. As a result,  $\text{Bi}_2\text{O}_3$  had better photocatalytic oxidation efficiency for  $\text{Hg}^0$  compared to the other two photocatalysts.

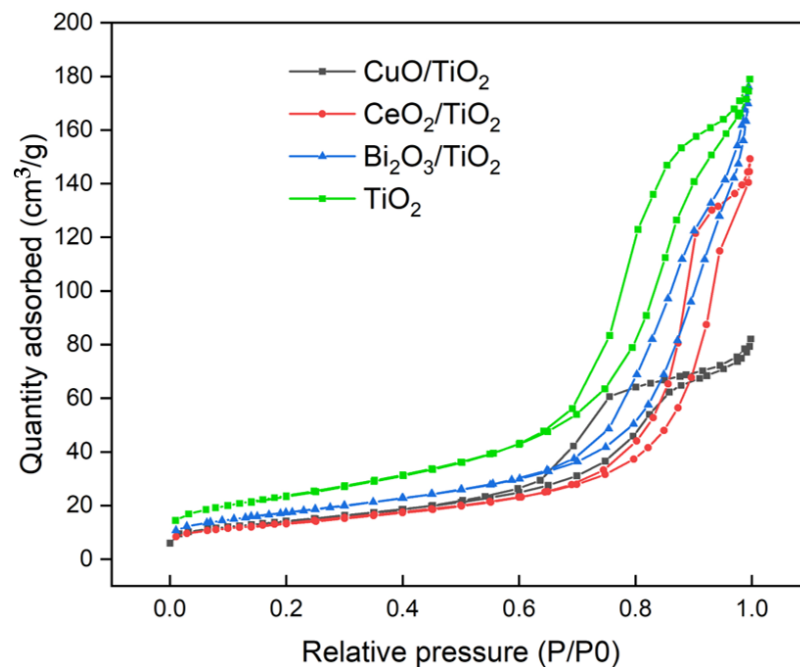


**Figure 1.**  $\text{N}_2$  adsorption–desorption isotherms of photocatalysts.

**Table 1.** Specific surface areas and average pore diameters of photocatalysts.

Type of Photocatalyst	Specific Surface Area ( $\text{m}^2/\text{g}$ )	Average Pore Diameter (nm)
$\text{TiO}_2$	85.29	9.91
$\text{CuO}/\text{TiO}_2$	48.16	9.65
$\text{CeO}_2/\text{TiO}_2$	50.82	10.15
$\text{Bi}_2\text{O}_3/\text{TiO}_2$	62.05	16.92

The morphologies of the prepared  $\text{TiO}_2$ ,  $\text{CuO}/\text{TiO}_2$ ,  $\text{CeO}_2/\text{TiO}_2$ , and  $\text{Bi}_2\text{O}_3/\text{TiO}_2$  were observed using FE-SEM as illustrated in Figure 2. The results of FE-SEM show that  $\text{TiO}_2$  and metal-oxide-modified  $\text{TiO}_2$  presented as nanoparticle agglomerations due to calcination during the preparation process. The EDS analysis depicts the atomic partition of each atom. The results show that the actual stoichiometry was not with the design in the synthesis process. This could be attributed to the limitation of EDS, in which the detection area was relatively small [25]. Figure 3 presents the mapping analysis of the photocatalysts,

which shows that various atoms were well distributed. Figure 4 presents the TEM analysis of the photocatalysts, showing the overlap between nanoparticles, creating a darker region. The crystal size of nanoparticles could be further estimated. As shown in Figure 4, the diameters of  $\text{TiO}_2$ ,  $\text{CuO}/\text{TiO}_2$ ,  $\text{CeO}_2/\text{TiO}_2$ , and  $\text{Bi}_2\text{O}_3/\text{TiO}_2$  were 15.5, 16.98, 20.15, and 21.27 nm, respectively.

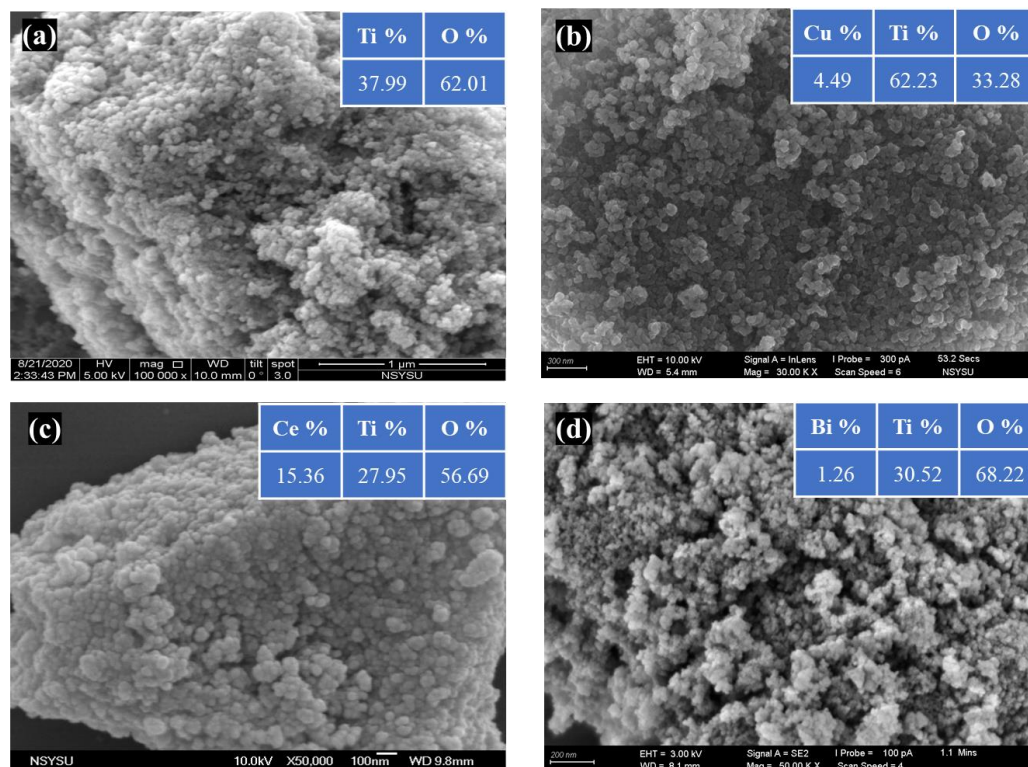


**Figure 2.** FE-SEM images and EDS results (atomic %) of (a)  $\text{TiO}_2$ , (b)  $\text{CuO}/\text{TiO}_2$ , (c)  $\text{CeO}_2/\text{TiO}_2$ , and (d)  $\text{Bi}_2\text{O}_3/\text{TiO}_2$ .

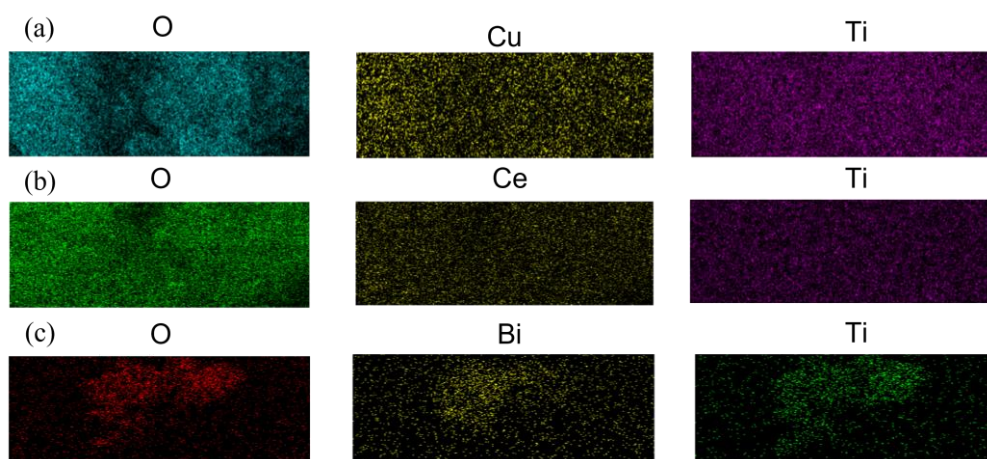


**Figure 3.** Mapping analysis of photocatalysts (a)  $\text{CuO}/\text{TiO}_2$ , (b)  $\text{CeO}_2/\text{TiO}_2$ , and (c)  $\text{Bi}_2\text{O}_3/\text{TiO}_2$ .

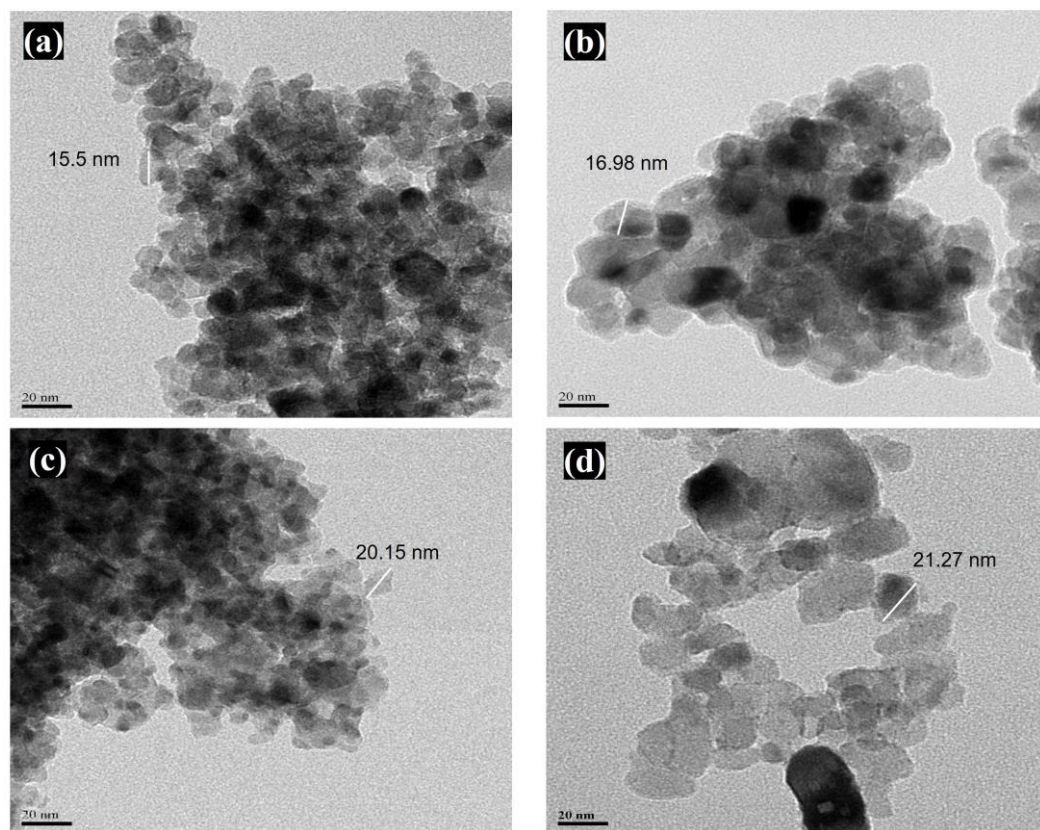


**Figure 4.** TEM images of (a)  $\text{TiO}_2$ , (b)  $\text{CuO}/\text{TiO}_2$ , (c)  $\text{CeO}_2/\text{TiO}_2$ , and (d)  $\text{Bi}_2\text{O}_3/\text{TiO}_2$ .

Figure 5 presents the XRD patterns of  $\text{TiO}_2$ ,  $\text{CuO}/\text{TiO}_2$ ,  $\text{CeO}_2/\text{TiO}_2$ , and  $\text{Bi}_2\text{O}_3/\text{TiO}_2$ .  $\text{TiO}_2$  had several characteristic peaks at  $2\theta = 25.39^\circ$ ,  $3.7.84^\circ$ ,  $48.09^\circ$ ,  $53.98^\circ$ ,  $62.79^\circ$ ,  $70.34^\circ$ , and  $75.10^\circ$  that were consistent with the Anatase  $\text{TiO}_2$  from the American Mineralogist Crystal Structure Database [26]. The crystallite sizes of the photocatalysts were calculated using the Scherrer equation [27]. Table 2 presents the results of crystallite sizes in the order  $\text{CeO}_2/\text{TiO}_2 > \text{Bi}_2\text{O}_3/\text{TiO}_2 > \text{CuO}/\text{TiO}_2 > \text{TiO}_2$ . Additionally, Figure 5 clearly shows the relatively low or undetected characteristic peaks of  $\text{CuO}$ ,  $\text{CeO}_2$ , and  $\text{Bi}_2\text{O}_3$ . Particularly, the characteristic peaks of  $\text{CuO}$  were not observed, while those of  $\text{CeO}_2$  and  $\text{Bi}_2\text{O}_3$  had relatively low intensity because the amounts of these metal oxides were too low to form crystals, with most of the photocatalysts in the amorphous state [28]. This might be attributed to the non-uniformly dispersed metal oxides over the Anatase  $\text{TiO}_2$ . Additionally, the atomic radius of  $\text{Cu}$  ( $\phi = 0.14 \text{ nm}$ ) was smaller than that of  $\text{Ti}$  ( $\phi = 0.187 \text{ nm}$ ), potentially causing two adverse effects [29]. First, excess  $\text{Cu}$  could enter the  $\text{TiO}_2$  lattice, thus decreasing the crystallinity of  $\text{TiO}_2$  and reducing the intensity of (101) facets of  $\text{TiO}_2$ . Second,  $\text{CuO}$  could easily block the inner pores of  $\text{TiO}_2$ , reducing the adsorptive capacity; this was consistent with the analytical BET results. Furthermore, overwhelmed metal oxides can accumulate over the surface of  $\text{TiO}_2$ , resulting in a decrease in light absorptivity and photocatalytic activity [19].

The photocatalysts absorbed incident light energy to excite electrons from the valence band to the conduction band. This left a hole in the valence band and an electron in the conduction band, thus creating electron/hole pairs. Photo-induced electrons and holes can further react with  $\text{O}_2$  and  $\text{H}_2\text{O}$  to produce reactive radicals  $\text{O}_2^-$  and  $\cdot\text{OH}$ , respectively, with high redox activity [30,31]. Therefore, the lifetime of the photo-induced electron/hole pair was the most important parameter for assessing the photocatalytic activity of the photocatalysts. Figure 6 presents the PL patterns of  $\text{TiO}_2$ ,  $\text{CuO}/\text{TiO}_2$ ,  $\text{CeO}_2/\text{TiO}_2$ , and  $\text{Bi}_2\text{O}_3/\text{TiO}_2$ . It demonstrates that  $\text{TiO}_2$  has the highest PL intensity, which was mainly attributed to the rapid recombination of electron/hole pairs, meaning that electrons could

not be transitioned from  $Ti^{3+}$  to  $O^-$  [32]. However, as  $TiO_2$  was modified with  $CuO$ ,  $CeO_2$ , and  $Bi_2O_3$ , the PL intensity decreased gradually, suggesting that the addition of metal oxides could effectively retard the recombination of electron/hole pairs and thus extend the lifetime of active species. For all the tested photocatalysts, the emission bands were observed mainly in the range of visible light ( $\lambda = 428\text{--}604\text{ nm}$ ). This could be attributed to the recombination of excited electrons with oxygen vacancies on the photocatalysts. On the other hand, a small peak appeared in the range of  $UV_A$  light, which is attributed to near-band emissions and the recombination of electron and hole pairs [33].

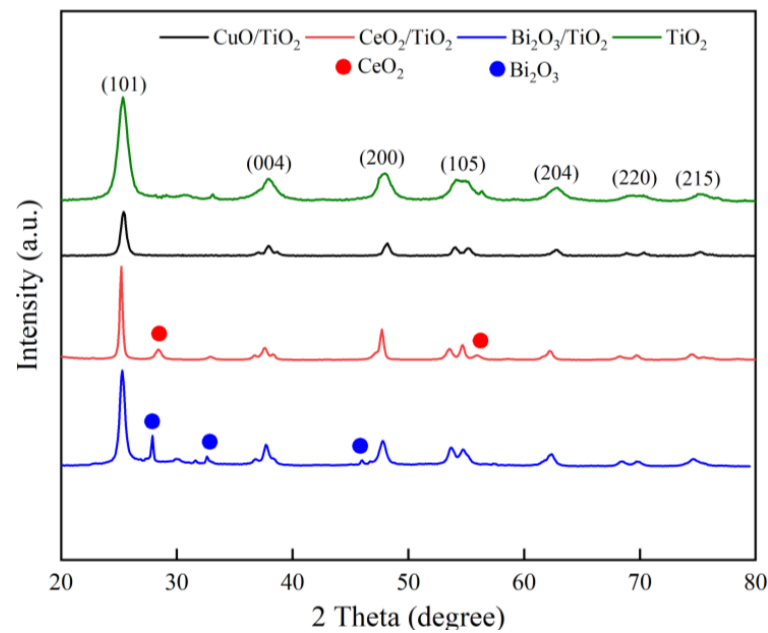


**Figure 5.** XRD analysis of  $TiO_2$ ,  $CuO/TiO_2$ ,  $CeO_2/TiO_2$ , and  $Bi_2O_3/TiO_2$ .

**Table 2.** Crystallite sizes calculated using the Debye Scherrer equation.

Photocatalysts	$TiO_2$	$CuO/TiO_2$	$CeO_2/TiO_2$	$Bi_2O_3/TiO_2$
Crystallite size (nm)	11.8	13.5	15.01	14.2

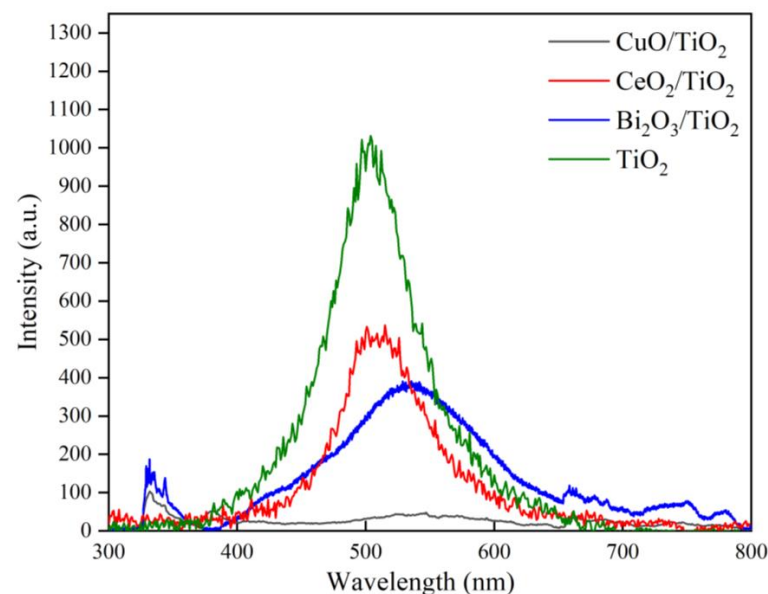


**Figure 6.** PL analysis of  $TiO_2$ ,  $CuO/TiO_2$ ,  $CeO_2/TiO_2$ , and  $Bi_2O_3/TiO_2$ .

Figure 7 illustrates the XPS spectra of Ti 2p over  $\text{TiO}_2$ ,  $\text{CuO}/\text{TiO}_2$ ,  $\text{CeO}_2/\text{TiO}_2$ , and  $\text{Bi}_2\text{O}_3/\text{TiO}_2$ . It shows two characteristic peaks at around 458 and 464 eV in the pristine  $\text{TiO}_2$ , attributed to  $\text{Ti } 2p_{3/2}$  and  $\text{Ti } 2p_{1/2}$ , respectively, also indicating that Ti appears in  $\text{Ti}^{4+}$ . After modification with metal oxides, the electron cloud around Ti decreased and the oxidation state decreased, leading to a shift of the peaks to lower binding energy [34]. Figure 8 depicts the characteristic peaks of metal oxides in the photocatalysts. Cu had two characteristic peaks at 933.8 and 953.4 eV, labeled  $\text{Cu } 2p_{3/2}$  and  $\text{Cu } 2p_{1/2}$ , respectively, with a binding energy gap of 19.6 eV, indicating that Cu was mainly in the form of  $\text{Cu}^{2+}$  instead of  $\text{Cu}^{1+}$  and  $\text{Cu}^0$  [35]. Ce 3d spectra were classified into  $\text{Ce } 3d_{3/2}$  and  $\text{Ce } 3d_{5/2}$ , labeled u and v, respectively. The peaks  $u^1$  and  $v^1$  corresponded to  $\text{Ce}^{4+}$ , while the peaks  $u, v, u^2, v^2, u^3,$  and  $v^3$  corresponded to  $\text{Ce}^{3+}$  [36]. The Bi 4f spectra showed that Bi was present as  $\text{Bi}^0$ , with two characteristic peaks at 154.9 and 160.2 eV, and  $\text{Bi}^{3+}$ , which exhibited two characteristic peaks at 157.2 and 162.5 eV [37]. Different valence states provide strong oxygen storage capacity, which can capture oxygen from the atmosphere and oxidize  $\text{Hg}^0$  to  $\text{Hg}^{2+}$ . Figure 9 presents the O 1s spectra of  $\text{TiO}_2$ ,  $\text{CuO}/\text{TiO}_2$ ,  $\text{CeO}_2/\text{TiO}_2$ , and  $\text{Bi}_2\text{O}_3/\text{TiO}_2$ . Herein,  $\text{O}_\alpha$  at a lower binding energy is assigned to lattice oxygen, while  $\text{O}_\beta$  at a higher binding energy is the chemisorbed oxygen and surface hydroxyl group, which has been reported to have higher activity to conduct oxidation reactions [38,39]. The integration area showed an increased proportion of  $\text{O}_\beta$  with the modification of metal oxides, further increasing  $\text{Hg}^0$  oxidation efficiency. Additionally, the increased binding energy compared with that of  $\text{TiO}_2$  indicated an increased oxidation state ( $\text{O}^{2-}$  to  $\text{O}^-$ ), which could enhance the photocatalytic oxidation of  $\text{Hg}^0$  [40].

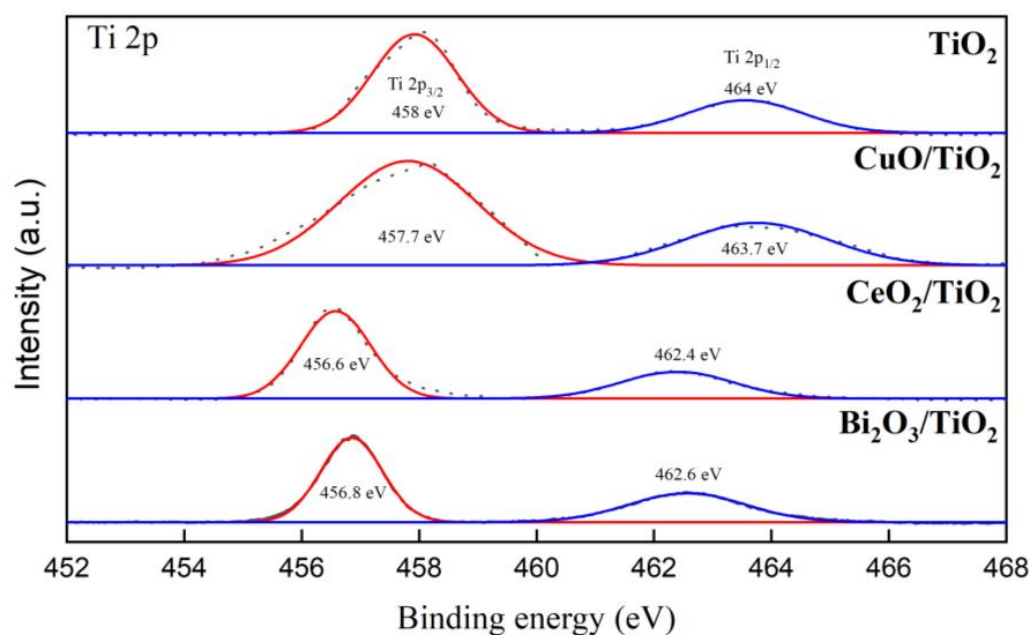


Figure 7. XPS spectra of Ti 2p over  $\text{TiO}_2$ ,  $\text{CuO}/\text{TiO}_2$ ,  $\text{CeO}_2/\text{TiO}_2$ , and  $\text{Bi}_2\text{O}_3/\text{TiO}_2$ .

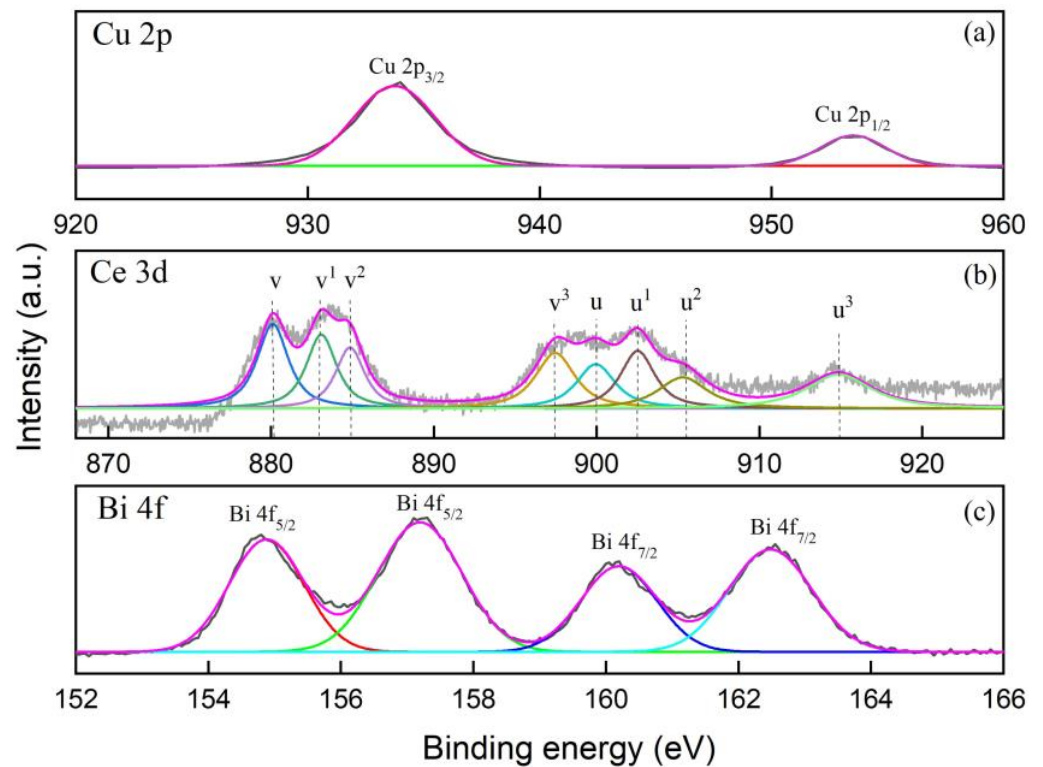


Figure 8. XPS analysis of metal components over (a) CuO/TiO<sub>2</sub>, (b) CeO<sub>2</sub>/TiO<sub>2</sub>, and (c) Bi<sub>2</sub>O<sub>3</sub>/TiO<sub>2</sub>.

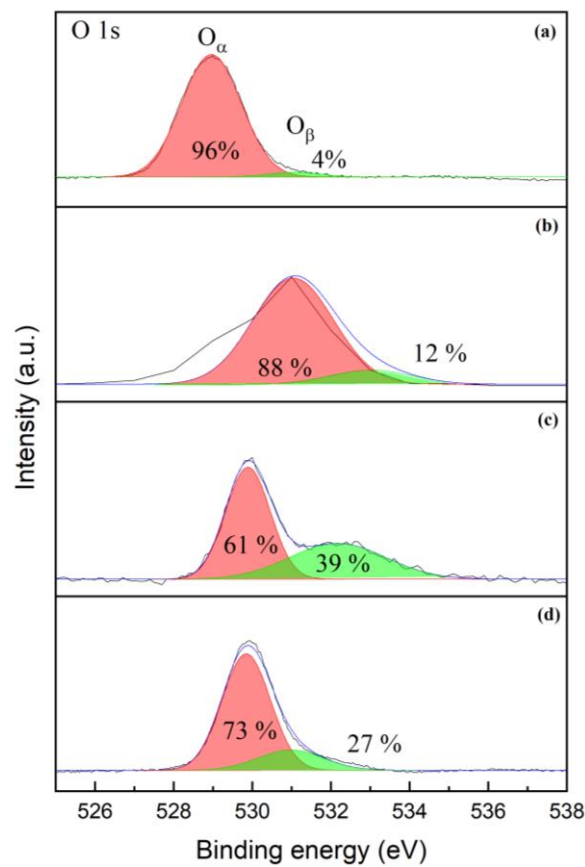
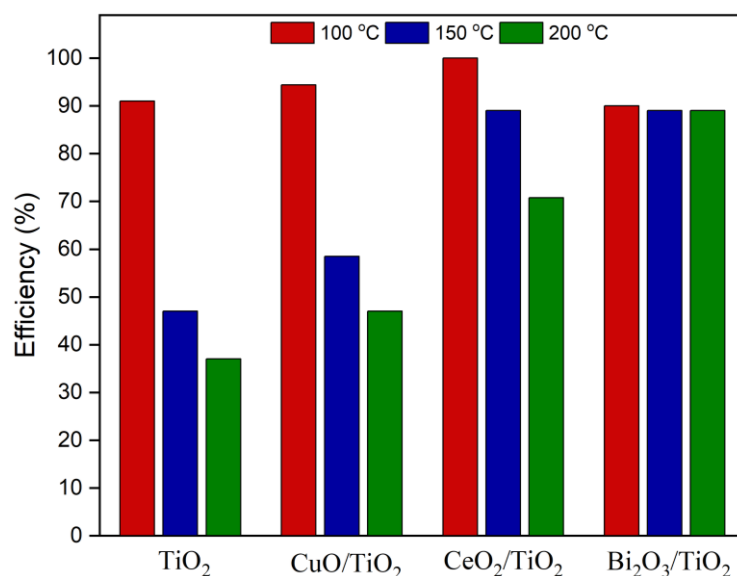


Figure 9. XPS spectra of O 1s over (a) TiO<sub>2</sub>, (b) CuO/TiO<sub>2</sub>, (c) CeO<sub>2</sub>/TiO<sub>2</sub>, and (d) Bi<sub>2</sub>O<sub>3</sub>/TiO<sub>2</sub>.

## 2.2. Effects of Different Modifying Materials on Photocatalytic Efficiency of $Hg^0$

Figure 10 illustrates the photocatalytic oxidation efficiencies of  $Hg^0$  in an  $N_2 + Hg^0$  atmosphere at reaction temperatures ranging from 100 to 200 °C for 2 h using  $TiO_2$ ,  $CuO/TiO_2$ ,  $CeO_2/TiO_2$ , and  $Bi_2O_3/TiO_2$ . The photocatalytic oxidation efficiencies of  $Hg^0$  for  $TiO_2$ ,  $CuO/TiO_2$ , and  $CeO_2/TiO_2$  decreased with reaction temperature. However, an opposite trend was observed for  $Bi_2O_3/TiO_2$ . The photocatalytic oxidation efficiencies of  $Hg^0$  for  $TiO_2$  was 91% at 100 °C and then dropped to 36% at 200 °C, showing a dramatic decrease of nearly 60% as reaction temperatures increased from 100 to 200 °C. However, after modifying using  $Bi_2O_3$ , the photocatalytic oxidation efficiency of  $Hg^0$  improved. To clarify the contribution of the photocatalytic and the traditional catalytic oxidation, we conducted continuous experiments, first without  $UV_A$  to let the catalyst react as a traditional thermal catalytic reaction. The catalytic oxidation efficiency of  $Hg^0$  reached its maximum after 30 min, as shown in Figure 11. As a catalyst,  $TiO_2$  had less than 5% of the catalytic oxidation efficiency of  $Hg^0$  without the irradiation of  $UV_A$ . By modifying  $TiO_2$  with metal oxides, the oxidation efficiency of  $Hg^0$  increased significantly.  $CuO/TiO_2$ ,  $CeO_2/TiO_2$ , and  $Bi_2O_3/TiO_2$  had the best catalytic oxidation efficiencies of  $Hg^0$  at 100 °C, which were 15%, 32%, and 52%, respectively. Secondly, we turn on  $UV_A$  to allow the materials to undergo the photocatalytic reaction. The photocatalytic reaction efficiencies of  $Hg^0$  increased dramatically for metal-oxide-modified  $TiO_2$ . The results showed that, for all the tested catalysts, photocatalysis contributed more than classical thermal catalysis. A previous study reported that  $TiO_2$  modified with metal oxide could yield more surface oxygen [41]. These findings concurred with the XPS analytical results obtained in this study. Equations (1)–(3) show the production of surface chemisorbed oxygen ( $O_\beta$ ) through the chemical reaction of metal oxides. Metal oxides can promote photocatalytic reactions, with their effectiveness in the order  $Bi_2O_3 > CeO_2 > CuO$ . At 200 °C,  $CuO/TiO_2$ ,  $CeO_2/TiO_2$ , and  $Bi_2O_3/TiO_2$  had performances of 47, 71, and 89%, respectively. Furthermore,  $Bi_2O_3$  exhibited excellent thermal stability, retaining almost the same oxidation efficiency at temperatures between 100 and 200 °C.



**Figure 10.** Photocatalytic efficiency of  $Hg^0$  under an atmosphere of  $N_2 + Hg^0$  with  $TiO_2$ ,  $CuO/TiO_2$ ,  $CeO_2/TiO_2$ , and  $Bi_2O_3/TiO_2$ .

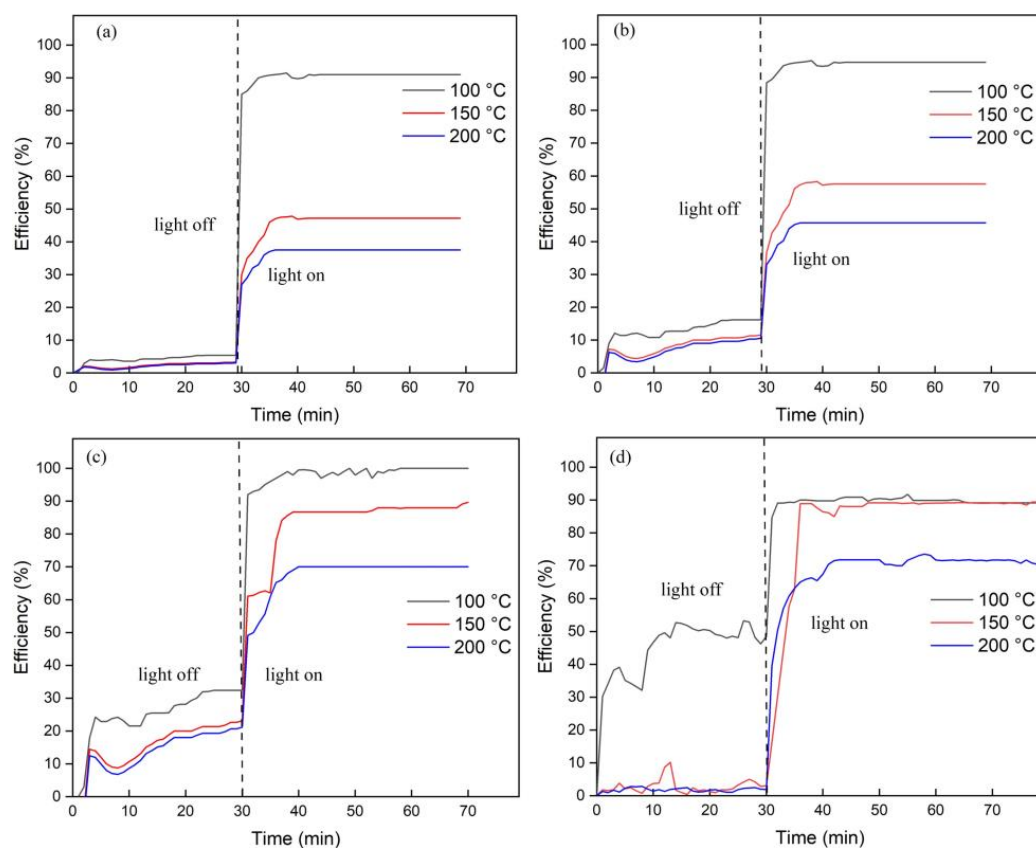


**Figure 11.** Photocatalytic efficiencies of  $Hg^0$  with and without  $UV_A$  of (a)  $TiO_2$ , (b)  $CuO/TiO_2$ , (c)  $CeO_2/TiO_2$ , (d)  $Bi_2O_3/TiO_2$ . (Dashed line is the time turn on the light).

### 2.3. Kinetic Modeling of the Photocatalytic Oxidation of $Hg^0$

The L–H kinetic mechanism was applied to simulate the photocatalytic oxidation efficiency of  $Hg^0$  [42]. In the context of a heterogeneous photocatalytic reaction, a decrease in  $K_{Hg^0}$  with the rise in the reaction temperature signified a chemical reaction characterized as physical adsorption. In contrast, an increase in  $K_{Hg^0}$  with reaction temperature characterized the chemical reaction as chemisorption, where adsorbed molecules form chemical bonds and adhere to the surface of the adsorbents [43].

As depicted in Table 3, an increase in reaction temperature led to an elevation in the  $k_r$  and a decrease in the value of  $K_{Hg^0}$ . This trend suggests that at higher reaction temperatures, the adsorption efficiency of  $Hg^0$  on the surface of photocatalysts diminishes. Based on the aforementioned outcomes, in this study, we inferred that physical adsorption predominantly governed the photocatalytic reactions of  $Hg^0$  for all the photocatalysts prepared. We further calculated the activation energy ( $E_a$ ) according to Arrhenius Law. The respective activation energies of  $TiO_2$ ,  $CuO/TiO_2$ ,  $CeO_2/TiO_2$ , and  $Bi_2O_3/TiO_2$  were 9.24, 2.54, 1.49, and 1.53 kcal/mol. These results indicate that the modification of metal oxides on  $TiO_2$  could effectively reduce the reaction barrier and improve the photocatalytic oxidation efficiency of  $Hg^0$  [44].

**Table 3.** Langmuir–Hinshelwood kinetic parameters for different photocatalysts.

Types of Photocatalysts	Reaction Temperatures (°C)	$K_{Hg}^0$ ( $m^3 \mu g^{-1}$ )	$k_r$ ( $\mu g m^2 min^{-1}$ )	$E_a$ ( $kcal mol^{-1}$ )
TiO <sub>2</sub>	100	9.264	0.341	9.24
	150	0.007	1.038	
	200	0.005	1.071	
CuO/TiO <sub>2</sub>	100	9.049	0.692	2.54
	150	0.268	0.940	
	200	0.234	1.52	
CeO <sub>2</sub> /TiO <sub>2</sub>	100	11.671	0.647	1.49
	150	4.843	0.894	
	200	0.778	1.331	
Bi <sub>2</sub> O <sub>3</sub> /TiO <sub>2</sub>	100	9.854	0.142	1.35
	150	1.069	0.429	
	200	0.192	1.238	

### 3. Materials and Methods

#### 3.1. Chemicals

The following chemical reagents were used for synthesizing metal-oxide-modified TiO<sub>2</sub>-based photocatalysts with no further purification, included titanium isopropoxide (ACROS ORGANICS, Waltham, MA, USA, Ti(OCH(CH<sub>3</sub>)<sub>2</sub>)<sub>4</sub>, 98%), copper nitrate (Alfa Aesar, Haverhill, MA, USA, Cu(NO<sub>3</sub>)<sub>2</sub>, 99.5%), cerium nitrate (Alfa Aesar, Ce(NO<sub>3</sub>)<sub>3</sub>·6H<sub>2</sub>O, 99.5%), bismuth nitrate (Alfa Aesar, Bi(NO<sub>3</sub>)<sub>3</sub>·5H<sub>2</sub>O, 99.5%), and isopropanol (Shimakyu's Pure Chemicals, Osaka, Japan).

#### 3.2. Preparation of Metal-Oxide-Modified TiO<sub>2</sub> Photocatalysts

Anatase TiO<sub>2</sub> was synthesized using the hydrothermal method [45]. First, 20 mL of titanium isopropoxide and 40 mL isopropanol were stirred for 1 h to form a uniform solution. Next, the solution was transferred to a Teflon container in an autoclave and kept in a furnace at 200 °C for 24 h. After the hydrothermal reactions, the solution was cleaned three times with DI water to remove organic compounds by centrifuging at 7000 × rpm for 10 min. The solution was then dried at 80 °C to remove the residual organic compounds and the dry precipitate was further calcined at 450 °C for 4 h to obtain TiO<sub>2</sub>.

The modification of CuO and CeO<sub>2</sub> to TiO<sub>2</sub> was further performed using an impregnation method [46]. The molar ratios of CuO/TiO<sub>2</sub> and CeO<sub>2</sub>/TiO<sub>2</sub> were 5% and 7%, respectively. Initially, certain amounts of metal oxide precursors were added to the solution of self-prepared TiO<sub>2</sub>, and DI water, and magnetically stirred for 12 h at room temperature. The solution was centrifuged to remove metal ions and the precipitate was then dried at 80 °C and calcined at 450 °C for 2 h. In this study, the molar ratio of Bi<sub>2</sub>O<sub>3</sub> and TiO<sub>2</sub> was 3%. Bi<sub>2</sub>O<sub>3</sub>/TiO<sub>2</sub> was synthesized using the hydrothermal method [47]. Bismuth nitrate was added to the solution of prepared TiO<sub>2</sub> and DI water and magnetically stirred for 1 h at room temperature. The solution was then transferred to the autoclave for a hydrothermal reaction at 180 °C for 24 h and then centrifuged to remove metal ions. The precipitate was further dried at 80 °C and then calcined at 450 °C for 4 h.

#### 3.3. Characterization Analysis of Photocatalysts

Surface characterization analysis of TiO<sub>2</sub>, CuO/TiO<sub>2</sub>, CeO<sub>2</sub>/TiO<sub>2</sub>, and Bi<sub>2</sub>O<sub>3</sub>/TiO<sub>2</sub> was performed using various physicochemical analytical instruments. The morphology and element dispersion of photocatalysts were observed using a field emission-scanning

electron microscope (FE-SEM, Zeiss, Oberkochen, Germany, Gemini 450), transmission electron microscope (TEM, Philips, Amsterdam, The Netherlands, CM-200 TWIN), and energy-dispersive X-ray spectroscopy (EDS, Zeiss, Germany, Oberkochen, Gemini 450). The specific surface area (SSA) of each photocatalyst was measured using a specific surface area analyzer (SSAA, Micromeritics, Norcross, GA, USA, ASAP2000). The crystallographic structures of the photocatalysts were analyzed using an X-ray diffractometer (XRD, Bruker, Billerica, MA, USA, D8 DISCOVER). The chemical compositions and valence states were analyzed using X-ray photoelectron spectroscopy (XPS, Philips, Amsterdam, The Netherlands Hybrid Quantera). The recombination times of photo-induced electron/hole pairs were estimated using photoluminescence (PL, Horiba, Kyoto, Japan, HR800). The band gap of each photocatalyst was analyzed using an ultraviolet-visible spectrometer (UV-Vis, Perkin-Elmer Precisely, Waltham, MA, US, Lambda 850).

### 3.4. Photocatalytic Activity of Self-Prepared Photocatalysts

For this particular study, a continuous flow photocatalytic reaction system comprising a standard gas generator, a mass flow controller, a mixing chamber, a photocatalytic reaction tube, and a real-time mercury monitor (NIC, EMP-2, measurement range = 0–1000  $\mu\text{g}/\text{m}^3$ , resolution = 0.1  $\mu\text{g}/\text{m}^3$ , and response time = 1 s) was established. A standard gas generator with a  $\text{Hg}^0$  permeation tube released the desired concentration of  $\text{Hg}^0$ , which was heated to 100 °C in an inert gas ( $\text{N}_2$ ) and further diluted with  $\text{N}_2$  and 6%  $\text{O}_2$  in the mixing chamber. The mixed gas was allowed to flow through the photocatalytic reactor to react with the photocatalysts coated on the surface of glass beads with 2 mm diameters. The photocatalytic reactor consisted of a photocatalytic reaction tube, with a black light of 365 nm wavelength (Sankyo Denki, BB-15W) in the middle of the reactor. The photocatalysts were placed between the reaction tube and the blacklight lamp. The blacklight lamps provided near-UV light of 15 W intensity and 365 nm wavelength. Additionally, the photocatalytic reaction tube was surrounded by a heating tape to maintain the photocatalytic reaction temperatures of 100, 150, and 200 °C.

Finally, the concentration of  $\text{Hg}^0$  at the inlet and outlet of the photocatalytic reactor was measured at a frequency of 1 plot/s. Calculating the concentration gradient between the inlet and outlet, the photocatalytic oxidation efficiency of  $\text{Hg}^0$  ( $\eta_{\text{Hg}^0}$ ) was further derived as shown in Equation (4). The mean and standard deviation (Mean  $\pm$  SD) were further calculated to describe the variation in the experimental data when the data reached the steady state.

$$\eta_{\text{Hg}^0} = \frac{\Delta \text{Hg}^0}{\text{Hg}_{in}^0} = \frac{\text{Hg}_{in}^0 - \text{Hg}_{out}^0}{\text{Hg}_{in}^0} \times 100\% \quad (4)$$

### 3.5. Langmuir–Hinshelwood (L–H) Kinetic Model

In this investigation, a Langmuir–Hinshelwood (L–H) kinetic model was applied to assess the correlation between the photocatalytic oxidation efficiency and the reaction rate of  $\text{Hg}^0$  across its various inlet concentrations. The adsorption equilibrium of  $\text{Hg}^0$  on the surface of photothermal catalysts was characterized by employing a Langmuir isotherm [48,49]. By considering the distribution of adsorbates on the surface of photocatalysts, the L–H kinetic model exhibited the reaction kinetics of the oxidation of  $\text{Hg}^0$ . This model helped elucidate the adsorption of  $\text{Hg}^0$  over the surface of photocatalysts and the activation energy of photocatalytic oxidation of  $\text{Hg}^0$ . By substituting inlet and outlet  $\text{Hg}^0$  concentrations into Equations (5) and (6), a linear correlation was derived, subsequently determining its intercept (Equation (7)) and slope (Equation (8)). This process allows us to deduce the reaction rate constant ( $k_r$ ) and the equilibrium constant ( $K_{\text{Hg}^0}$ ) of the photocatalytic reaction of  $\text{Hg}^0$  using a straight line plot of  $r^{-1}$  (herein,  $r$  represents reaction rate) versus  $C_{\text{Hg}^0}^{-1}$ .

$$r = \frac{k_r (K_{\text{Hg}^0} C_{\text{Hg}^0})}{1 + K_{\text{Hg}^0} C_{\text{Hg}^0}} \quad (5)$$

$$\frac{1}{r} = \frac{1}{k_r} + \left(\frac{1}{k_r K_{Hg^0}}\right) \left(\frac{1}{C_{Hg^0}}\right) \quad (6)$$

$$\frac{1}{k_r} = \text{intercept} \quad (7)$$

$$\frac{1}{k_r K_{Hg^0}} = \text{slope} \quad (8)$$

#### 4. Conclusions

In this study, three metal oxides ( $\text{CuO}_2$ ,  $\text{CeO}_2$ , and  $\text{Bi}_2\text{O}_3$ ) were employed to modify  $\text{TiO}_2$  in order to enhance the photocatalytic oxidation efficiency of  $\text{Hg}^0$ . While the modification of metal oxides might have blocked the pore structure of anatase  $\text{TiO}_2$ , it significantly reduced the PL intensity, which benefitted photocatalytic oxidation reactions. Moreover, the catalysts under modification exhibited a higher partition of chemisorbed oxygen. At 200 °C, these two enhancements could effectively improve the photocatalytic oxidation efficiency of  $\text{Hg}^0$  in the following order:  $\text{Bi}_2\text{O}_3/\text{TiO}_2 > \text{CeO}_2/\text{TiO}_2 > \text{CuO}/\text{TiO}_2 > \text{TiO}_2$ . Based on the comparison of catalytic (light off) and photocatalytic (light on) oxidation experiments of  $\text{Hg}^0$ , we revealed that  $\text{Bi}_2\text{O}_3/\text{TiO}_2$  was the best composite to photocatalytically oxidize  $\text{Hg}^0$  at 100–200 °C compared with  $\text{CeO}_2/\text{TiO}_2$  and  $\text{CuO}/\text{TiO}_2$ . The innovative findings obtained in this study were mainly attributed to the fact that  $\text{Bi}_2\text{O}_3/\text{TiO}_2$  had a higher specific surface area, which could enrich more chemisorbed oxygen on its surface, compared with  $\text{CuO}/\text{TiO}_2$  and  $\text{CeO}_2/\text{TiO}_2$ . The simulation of the L–H kinetic model revealed that the overall  $\text{Hg}^0$  photocatalytic reaction was dominated by physical adsorption. Furthermore, another novelty of this study was to inter-compare the activation energy ( $E_a$ ) based on the Arrhenius Law. It showed that the activation energies of  $\text{TiO}_2$ ,  $\text{CuO}/\text{TiO}_2$ ,  $\text{CeO}_2/\text{TiO}_2$ , and  $\text{Bi}_2\text{O}_3/\text{TiO}_2$  were 9.24, 2.54, 1.49, and 1.35 kcal/mole, respectively, and the energy barriers were reduced significantly by metal oxide modification. We thus concluded that  $\text{Bi}_2\text{O}_3/\text{TiO}_2$  was the best photocatalyst because it had the highest photocatalytic oxidation of  $\text{Hg}^0$ .

**Author Contributions:** C.-S.Y. planned and guided the experimental study; J.-R.Z. performed the research and analyzed/summarized the experimental data. The manuscript was written by J.-R.Z. and proofread by C.-S.Y., with contribution from the co-author. All authors have read and agreed to the published version of the manuscript.

**Funding:** This study was performed under the auspices of the Ministry of Science and Technology (MOST) of ROC (Taiwan), which financially funded the research project (MOST 111-2221-E-110-009). The authors are grateful to MOST for its constant financial support.

**Data Availability Statement:** Raw data are available from the corresponding author upon request.

**Conflicts of Interest:** The authors declare no conflicts of interest.

#### Nomenclature

Abbreviation	Definition
AC	activated carbon
$\text{Bi}_2\text{O}_3/\text{TiO}_2$	$\text{Bi}_2\text{O}_3$ modified $\text{TiO}_2$
$\text{CeO}_2/\text{TiO}_2$	$\text{CeO}_2$ modified $\text{TiO}_2$
$C_{Hg^0}$	concentration of gas-phase $\text{Hg}^0$
CFPPs	coal-fired power plants
$\text{CuO}/\text{TiO}_2$	$\text{CuO}$ modified $\text{TiO}_2$
$E_a$	activation energy
EDS	energy-dispersive X-ray spectroscopy
ESP	electrostatic precipitator
FE-SEM	field emission-scanning electron microscope
$K_{Hg^0}$	equilibrium constant of photocatalytic reaction of $\text{Hg}^0$
$k_r$	reaction rate constant of photocatalytic reaction of $\text{Hg}^0$

Abbreviation	Definition
L–H	Langmuir–Hinshelwood
O <sub>α</sub>	lattice oxygen
O <sub>β</sub>	chemisorbed oxygen
PL	photoluminescence
SCR	selective catalytic reduction
SD	standard deviation
SSA	specific surface area
SSAA	specific surface area analyzer
TEM	transmission electron microscope
UV	ultraviolet
UV-Vis	ultraviolet-visible spectrometer
WFGD	wet flue gas desulfurization
XPS	X-ray photoelectron spectroscopy
XRD	X-ray diffractometer

## References

1. UNEP. Global mercury assessment 2018. In *UN Environment Programme; Chemicals and Health Branch*: Geneva, Switzerland, 2019.
2. Cediell Ulloa, A.; Gliga, A.; Love, T.M.; Pineda, D.; Mruzek, D.W.; Watson, G.E.; Davidson, P.W.; Shamlaye, C.F.; Strain, J.J.; Myers, G.J.; et al. Prenatal methylmercury exposure and DNA methylation in seven-year-old children in the Seychelles Child Development Study. *Environ. Int.* **2021**, *147*, 106321. [[CrossRef](#)] [[PubMed](#)]
3. The Lancet. Minamata Convention on mercury: A contemporary reminder. *Lancet* **2017**, *390*, 822. [[CrossRef](#)] [[PubMed](#)]
4. Pirrone, N.; Cinnirella, S.; Feng, X.; Finkelman, R.B.; Friedli, H.R.; Leaner, J.; Mason, R.; Mukherjee, A.B.; Stracher, G.B.; Streets, D. Global mercury emissions to the atmosphere from anthropogenic and natural sources. *Atmos. Chem. Phys.* **2010**, *10*, 5951–5964. [[CrossRef](#)]
5. Cheng, C.-M.; Cao, Y.; Kai, Z.; Pan, W.-P. Co-effects of sulfur dioxide load and oxidation air on mercury re-emission in forced-oxidation limestone flue gas desulfurization wet scrubber. *Fuel* **2013**, *106*, 505–511. [[CrossRef](#)]
6. Zhang, Y.; Yang, J.; Yu, X.; Sun, P.; Zhao, Y.; Zhang, J.; Chen, G.; Yao, H.; Zheng, C. Migration and emission characteristics of Hg in coal-fired power plant of China with ultra low emission air pollution control devices. *Fuel Process. Technol.* **2017**, *158*, 272–280. [[CrossRef](#)]
7. Yang, J.; Na, Y.; Hu, Y.; Zhu, P.; Meng, F.; Guo, Q.; Yang, Z.; Qu, W.; Li, H. Granulation of Mn-based perovskite adsorbent for cyclic Hg<sup>0</sup> capture from coal combustion flue gas. *Chem. Eng. J.* **2023**, *459*, 141679. [[CrossRef](#)]
8. Zhang, Y.; Zhao, Y.; Xiong, Z.; Gao, T.; Xiao, R.; Liu, P.; Liu, J.; Zhang, J. Photo- and thermo-catalytic mechanisms for elemental mercury removal by Ce doped commercial selective catalytic reduction catalyst (V<sub>2</sub>O<sub>5</sub>/TiO<sub>2</sub>). *Chemosphere* **2022**, *287*, 132336. [[CrossRef](#)]
9. Snider, G.; Ariya, P. Photo-catalytic oxidation reaction of gaseous mercury over titanium dioxide nanoparticle surfaces. *Chem. Phys. Lett.* **2010**, *491*, 23–28. [[CrossRef](#)]
10. Szymaszek, A.; Samojedon, B.; Motak, M. The Deactivation of Industrial SCR Catalysts—A Short Review. *Energies* **2020**, *13*, 3870. [[CrossRef](#)]
11. Pu, Y.; Xie, X.; Jiang, W.; Yang, L.; Jiang, X.; Yao, L. Low-temperature selective catalytic reduction of NO<sub>x</sub> with NH<sub>3</sub> over zeolite catalysts: A review. *Chin. Chem. Lett.* **2020**, *31*, 2549–2555. [[CrossRef](#)]
12. Barreca, D.; Carraro, G.; Gasparotto, A.; Maccato, C.; Warwick, M.E.A.; Kaunisto, K.; Sada, C.; Turner, S.; Gönüllü, Y.; Ruoko, T.-P.; et al. Fe<sub>2</sub>O<sub>3</sub>-TiO<sub>2</sub> Nano-heterostructure Photoanodes for Highly Efficient Solar Water Oxidation. *Adv. Mater. Interfaces* **2015**, *2*, 1500313. [[CrossRef](#)]
13. Zheng, J.-R.; Yuan, C.-S.; Ie, I.-R.; Shen, H. S-scheme heterojunction CeO<sub>2</sub>/TiO<sub>2</sub> modified by reduced graphene oxide (rGO) as charge transfer route for integrated photothermal catalytic oxidation of Hg<sup>0</sup>. *Fuel* **2023**, *343*, 127973. [[CrossRef](#)]
14. Zhou, Q.; He, K.; Wang, X.; Lim, K.H.; Liu, P.; Wang, W.; Wang, Q. Investigation on the redox/acidic features of bimetallic MOF-derived CeMOx catalysts for low-temperature NH<sub>3</sub>-SCR of NO<sub>x</sub>. *Appl. Catal. A Gen.* **2022**, *643*, 118796. [[CrossRef](#)]
15. Zhang, G.; Song, A.; Duan, Y.; Zheng, S. Enhanced photocatalytic activity of TiO<sub>2</sub>/zeolite composite for abatement of pollutants. *Microporous Mesoporous Mater.* **2018**, *255*, 61–68. [[CrossRef](#)]
16. Park, H.; Park, Y.; Kim, W.; Choi, W. Surface modification of TiO<sub>2</sub> photocatalyst for environmental applications. *J. Photochem. Photobiol. C Photochem. Rev.* **2013**, *15*, 1–20. [[CrossRef](#)]
17. Mei, Q.; Zhang, F.; Wang, N.; Yang, Y.; Wu, R.; Wang, W. TiO<sub>2</sub>/Fe<sub>2</sub>O<sub>3</sub> heterostructures with enhanced photocatalytic reduction of Cr(vi) under visible light irradiation. *RSC Adv.* **2019**, *9*, 22764–22771. [[CrossRef](#)] [[PubMed](#)]
18. Li, L.; Chen, X.; Quan, X.; Qiu, F.; Zhang, X. Synthesis of CuO<sub>x</sub>/TiO<sub>2</sub> Photocatalysts with Enhanced Photocatalytic Performance. *ACS Omega* **2023**, *8*, 2723–2732. [[CrossRef](#)] [[PubMed](#)]
19. Wu, J.; Li, C.; Zhao, X.; Wu, Q.; Qi, X.; Chen, X.; Hu, T.; Cao, Y. Photocatalytic oxidation of gas-phase Hg<sup>0</sup> by CuO/TiO<sub>2</sub>. *Appl. Catal. B Environ.* **2015**, *176–177*, 559–569. [[CrossRef](#)]
20. Shen, H.; Huang, X.-W.; Ie, I.-R.; Yuan, C.-S.; Wang, S.-W. Enhancement of Oxidation Efficiency of Elemental Mercury by CeO<sub>2</sub>/TiO<sub>2</sub> at Low Temperatures Governed by Different Mechanisms. *ACS Omega* **2020**, *5*, 1796–1804. [[CrossRef](#)] [[PubMed](#)]

21. Li, H.; Wu, C.-Y.; Li, Y.; Zhang, J. CeO<sub>2</sub>-TiO<sub>2</sub> Catalysts for Catalytic Oxidation of Elemental Mercury in Low-Rank Coal Combustion Flue Gas. *Environ. Sci. Technol.* **2011**, *45*, 7394–7400. [[CrossRef](#)]
22. Zhang, Y.; Lu, J.; Hoffmann, M.R.; Wang, Q.; Cong, Y.; Wang, Q.; Jin, H. Synthesis of g-C<sub>3</sub>N<sub>4</sub>/Bi<sub>2</sub>O<sub>3</sub>/TiO<sub>2</sub> composite nanotubes: Enhanced activity under visible light irradiation and improved photoelectrochemical activity. *RSC Adv.* **2015**, *5*, 48983–48991. [[CrossRef](#)]
23. Thommes, M.; Kaneko, K.; Neimark, A.V.; Olivier, J.P.; Rodriguez-Reinoso, F.; Rouquerol, J.; Sing, K.S.W. Physisorption of gases, with special reference to the evaluation of surface area and pore size distribution (IUPAC Technical Report). *Pure Appl. Chem.* **2015**, *87*, 1051–1069. [[CrossRef](#)]
24. Zhang, Y.; Wu, K.; Yang, Z.; Ye, G. A reappraisal of the ink-bottle effect and pore structure of cementitious materials using intrusion-extrusion cyclic mercury porosimetry. *Cem. Concr. Res.* **2022**, *161*, 106942. [[CrossRef](#)]
25. Gnanaseelan, N.; Latha, M.; Mantilla, A.; Sathish-Kumar, K.; Caballero-Briones, F. The role of redox states and junctions in photocatalytic hydrogen generation of MoS<sub>2</sub>-TiO<sub>2</sub>-rGO and CeO<sub>2</sub>-Ce<sub>2</sub>Ti<sub>3</sub>O<sub>8,7</sub>-TiO<sub>2</sub>-rGO composites. *Mater. Sci. Semicond. Process.* **2020**, *118*, 105185. [[CrossRef](#)]
26. Yu, R.; Yang, Y.; Zhou, Z.; Li, X.; Gao, J.; Wang, N.; Li, J.; Liu, Y. Facile synthesis of ternary heterojunction Bi<sub>2</sub>O<sub>3</sub>/reduced graphene oxide/TiO<sub>2</sub> composite with boosted visible-light photocatalytic activity. *Sep. Purif. Technol.* **2022**, *299*, 121712. [[CrossRef](#)]
27. Scherrer, P. Bestimmung der Größe und der inneren Struktur von Kolloidteilchen mittels Röntgenstrahlen. *Nachrichten Ges. Wiss. Göttingen Math.-Phys. Kl.* **1918**, *1918*, 98–100.
28. Zheng, J.-R.; Yuan, C.-S.; Ie, I.-R.; Shen, H.; Hung, C.-H. Cutting-edge technologies developing for removal of Hg<sup>0</sup> and/or NO<sub>x</sub>—A critical review of graphene-assisted catalysts. *Chem. Eng. J.* **2023**, *474*, 145898. [[CrossRef](#)]
29. Tuo, Y.-X.; Shi, L.-J.; Cheng, H.-Y.; Zhu, Y.-A.; Yang, M.-L.; Xu, J.; Han, Y.-F.; Li, P.; Yuan, W.-K. Insight into the support effect on the particle size effect of Pt/C catalysts in dehydrogenation. *J. Catal.* **2018**, *360*, 175–186. [[CrossRef](#)]
30. Gao, C.; Shi, J.-W.; Fan, Z.; Wang, B.; Wang, Y.; He, C.; Wang, X.; Li, J.; Niu, C. “Fast SCR” reaction over Sm-modified MnO<sub>x</sub>-TiO<sub>2</sub> for promoting reduction of NO<sub>x</sub> with NH<sub>3</sub>. *Appl. Catal. A Gen.* **2018**, *564*, 102–112. [[CrossRef](#)]
31. Yang, J.-Z.; Ie, I.-R.; Lin, Z.-B.; Yuan, C.-S.; Shen, H.; Shih, C.-H. Oxidation efficiency and reaction mechanisms of gaseous elemental mercury by using CeO<sub>2</sub>/TiO<sub>2</sub> and CuO/TiO<sub>2</sub> photo-oxidation catalysts at low temperatures in multi-pollutant environments. *J. Taiwan Inst. Chem. Eng.* **2021**, *125*, 413–423. [[CrossRef](#)]
32. Ie, I.-R.; Zheng, J.-R.; Yuan, C.-S.; Shih, C.-H.; Lin, Z.-B. Photo-oxidation and kinetics of gaseous elemental mercury using CeO<sub>2</sub>/TiO<sub>2</sub>{001} and {101} photocatalysts in the atmosphere of multiple air pollutants. *J. Environ. Chem. Eng.* **2022**, *10*, 107411. [[CrossRef](#)]
33. Baran Aydın, E.; Ateş, S.; Sığırçık, G. CuO-TiO<sub>2</sub> nanostructures prepared by chemical and electrochemical methods as photo electrode for hydrogen production. *Int. J. Hydrogen Energy* **2022**, *47*, 6519–6534. [[CrossRef](#)]
34. Cao, Y.; Li, Q.; Li, C.; Li, J.; Yang, J. Surface heterojunction between (001) and (101) facets of ultrafine anatase TiO<sub>2</sub> nanocrystals for highly efficient photoreduction CO<sub>2</sub> to CH<sub>4</sub>. *Appl. Catal. B* **2016**, *198*, 378–388. [[CrossRef](#)]
35. Zhang, S.; Gong, X.; Shi, Q.; Ping, G.; Xu, H.; Waleed, A.; Li, G. CuO Nanoparticle-Decorated TiO<sub>2</sub>-Nanotube Heterojunctions for Direct Synthesis of Methyl Formate via Photo-Oxidation of Methanol. *ACS Omega* **2020**, *5*, 15942–15948. [[CrossRef](#)] [[PubMed](#)]
36. Tuyen, L.T.T.; Quang, D.A.; Tam Toan, T.T.; Tung, T.Q.; Hoa, T.T.; Mau, T.X.; Khieu, D.Q. Synthesis of CeO<sub>2</sub>/TiO<sub>2</sub> nanotubes and heterogeneous photocatalytic degradation of methylene blue. *J. Environ. Chem. Eng.* **2018**, *6*, 5999–6011. [[CrossRef](#)]
37. Huang, Y.; Wei, Y.; Wang, J.; Luo, D.; Fan, L.; Wu, J. Controllable fabrication of Bi<sub>2</sub>O<sub>3</sub>/TiO<sub>2</sub> heterojunction with excellent visible-light responsive photocatalytic performance. *Appl. Surf. Sci.* **2017**, *423*, 119–130. [[CrossRef](#)]
38. Liu, H.; Su, Y.; Hu, H.; Cao, W.; Chen, Z. An ionic liquid route to prepare mesoporous ZrO<sub>2</sub>-TiO<sub>2</sub> nanocomposites and study on their photocatalytic activities. *Adv. Powder Technol.* **2013**, *24*, 683–688. [[CrossRef](#)]
39. Li, M.; Wang, P.; Ji, Z.; Zhou, Z.; Xia, Y.; Li, Y.; Zhan, S. Efficient photocatalytic oxygen activation by oxygen-vacancy-rich CeO<sub>2</sub>-based heterojunctions: Synergistic effect of photoexcited electrons transfer and oxygen chemisorption. *Appl. Catal. B Environ.* **2021**, *289*, 120020. [[CrossRef](#)]
40. Guo, Z.; Jing, G.; Tolba, S.A.; Yuan, C.-s.; Li, Y.-H.; Zhang, X.; Huang, Z.; Zhao, H.; Wu, X.; Shen, H.; et al. Design and construction of an O-Au-O coordination environment in Au single atom-doped Ti<sup>4+</sup> defected TiO<sub>2</sub> for an enhanced oxidative ability of lattice oxygen for Hg<sup>0</sup> oxidation. *Chem. Eng. J.* **2023**, *451*, 138895. [[CrossRef](#)]
41. Ie, I.-R.; Zheng, J.-R.; Yuan, C.-S.; Lin, Z.-B.; Shih, C.-H.; Shen, H. Surface characteristics of innovative TiO<sub>2</sub>{001} and CeO<sub>2</sub>/TiO<sub>2</sub>{001} catalysts and simultaneous removal of elemental mercury and nitric oxide at low temperatures. *Fuel* **2022**, *317*, 123479. [[CrossRef](#)]
42. Zheng, J.-R.; Ie, I.-R.; Wang, S.-W.; Yuan, C.-S.; Shen, H.-Z.; Li, Y.-H. Enhancing the oxidation efficiency of elemental mercury in the presence of NO and SO<sub>2</sub> by using Cu(II)O doped TiO<sub>2</sub> photothermal catalysts: Kinetics and mechanisms. *Fuel* **2023**, *331*, 125850. [[CrossRef](#)]
43. Zhang, Q.; Mei, J.; Sun, P.; Zhao, H.; Guo, Y.; Yang, S. Mechanism of Elemental Mercury Oxidation over Copper-Based Oxide Catalysts: Kinetics and Transient Reaction Studies. *Ind. Eng. Chem. Res.* **2020**, *59*, 61–70. [[CrossRef](#)]
44. Gao, F.; Tang, X.; Yi, H.; Zhao, S.; Li, C.; Li, J.; Shi, Y.; Meng, X. A review on selective catalytic reduction of NO<sub>x</sub> by NH<sub>3</sub> over Mn-Based catalysts at low temperatures: Catalysts, mechanisms, kinetics and DFT calculations. *Catalysts* **2017**, *7*, 199. [[CrossRef](#)]
45. Yang, H.G.; Liu, G.; Qiao, S.Z.; Sun, C.H.; Jin, Y.G.; Smith, S.C.; Zou, J.; Cheng, H.M.; Lu, G.Q. Solvothermal Synthesis and Photoreactivity of Anatase TiO<sub>2</sub> Nanosheets with Dominant {001} Facets. *J. Am. Chem. Soc.* **2009**, *131*, 4078–4083. [[CrossRef](#)] [[PubMed](#)]
46. Zagaynov, I.V.; Liberman, E.Y.; Prikhodko, O.P.; Kon’kova, T.V. Catalytic activity of CeO<sub>2</sub>@TiO<sub>2</sub> for environmental protection. *New J. Chem.* **2024**, *48*, 2842–2848. [[CrossRef](#)]

47. Malligavathy, M.; Iyyapushpam, S.; Nishanthi, S.T.; Pathinettam Padiyan, D. Remarkable catalytic activity of Bi<sub>2</sub>O<sub>3</sub>/TiO<sub>2</sub> nanocomposites prepared by hydrothermal method for the degradation of methyl orange. *J. Nanopart. Res.* **2017**, *19*, 144. [[CrossRef](#)]
48. Ishag, A.; Yue, Y.; Xiao, J.; Huang, X.; Sun, Y. Recent advances on the adsorption and oxidation of mercury from coal-fired flue gas: A review. *J. Clean. Prod.* **2022**, *367*, 133111. [[CrossRef](#)]
49. Wang, C.; Hong, Q.; Ma, C.; Mei, J.; Yang, S. Novel Promotion of Sulfuration for Hg<sup>0</sup> Conversion over V<sub>2</sub>O<sub>5</sub>-MoO<sub>3</sub>/TiO<sub>2</sub> with HCl at Low Temperatures: Hg<sup>0</sup> Adsorption, Hg<sup>0</sup> Oxidation, and Hg<sup>2+</sup> Adsorption. *Environ. Sci. Technol.* **2021**, *55*, 7072–7081. [[CrossRef](#)] [[PubMed](#)]

**Disclaimer/Publisher's Note:** The statements, opinions and data contained in all publications are solely those of the individual author(s) and contributor(s) and not of MDPI and/or the editor(s). MDPI and/or the editor(s) disclaim responsibility for any injury to people or property resulting from any ideas, methods, instructions or products referred to in the content.